Design and development of a portable beta spectrometer for 90Sr measurement in contaminated matrices

Julien Venara, Mehdi Ben Mosbah, Charly Mahe, Julien Astier, Susanna Adera, Marie Cuozzo, Vincent Goudeau

Design and development of a portable β- spectrometer for ^{90}Sr activity measurements in contaminated matrices

J. Venara[a]*, M. Ben Mosbah[b], C. Mahé[a], J. Astier[a], S. Adera[a], M. Cuozzo[a], V. Goudeau[c],

[a] CEA, DEN, DE2D, SEAD, LSTD, F-30207 Bagnols-sur-Cèze, France.
[b] CEA, DEN, DTN, SMTA, LMN, F-13108 Saint-Paul-lez-Durance, France.
[c] CEA, LE RIPAULT, F-37260 Monts, France.

* Corresponding author. Tel.: +33466397806

E-mail address: julien.venara@cea.fr (J. Venara).

ABSTRACT

Determining the nature and activity of radionuclides is an important task in the nuclear industry. Pure β- emitters are hard to characterize because the mean free path of electrons in dense matter is very short. Most measurement techniques are therefore based on destructive laboratory analyses. This article presents a non-destructive approach based on a portable β- spectrometer, designed to provide qualitative and quantitative information on pure β- emitters, notably ^{90}Sr. Building on existing methods focused on the measurement of ^{90}Sr activity in natural soil contaminated by the Chernobyl accident, the aim of this project is to develop a detector for the radiological characterization of different types of contaminated matrices, in particular the contaminated concrete structures typically found in nuclear facilities. A measurement device equipped with an EJ200 plastic scintillator was designed using Monte Carlo simulations with the MCNP6 and PENELOPE calculation codes. The energy calibration and the response of the detector were determined using experimental measurements and MCNP simulations of laboratory configurations of standard β- sources. These data were used to validate the model of the detector, as well as to determine calibration coefficients by numerical simulation for various on-site measurement configurations. The device was then used to characterize samples of sand from a decommissioning site in France (Fontenay-aux-Roses). The resulting ^{90}Sr activities are within experimental uncertainties of those obtained using destructive measurements. These results are promising for wider applications on nuclear decommissioning sites.

Keywords: ^{90}Sr; Beta spectrometry; Decommissioning; Contaminated matrices; Monte Carlo; Scintillation detector

Non-standard abbreviations: none.

Declarations of interest: none.

1. Introduction

The number of nuclear decommissioning sites is ever increasing worldwide. The management of radioactive information is a crucial aspect of many of the major components of these projects: radioactive waste management, choice of decontamination solutions, operator radioprotection. The radiological state of buildings and equipment can be established by combining non-destructive on-site radioactivity measurements with numerical modeling.

The characterization of ɣ emitters can be done by gamma-ray spectrometry, combined in some cases with gamma imaging. In simple situations in which the characteristic spectrum is known, the activity of all the other radionuclides, notably pure β- emitters, can be determined using data on the main ɣ emitters such as ^{137}Cs and ^{60}Co, which act as radioactive tracers. This procedure is unfeasible however in more complicated cases, such as for soils or buildings, in which the ^{137}Cs/^{90}Sr ratio can vary substantially. In the soils and rivers contaminated by the Chernobyl accident for instance, ^{137}Cs/^{90}Sr ratios were found to vary from 0.5 to 0.01 [1], in part because the two radionuclides have different transport rates in these materials. The radiological inventory becomes very uncertain or even impossible to draw up and an alternative approach is required.

Pure β- emitters such as ^{90}Sr cannot be detected using gamma spectrometry. Currently, measurements of ^{90}Sr activity are almost exclusively performed by radiochemical analysis of extracted samples. These radiochemical analyses have several drawbacks. First, they are

53 destructive and involve several sample preparation steps (dilution, concentration, separation
54 of the interfering radionuclides) that are problematic for the representativity of the samples.
55 For the results to be interpretable moreover, the analyses have to be repeated on a large
56 number of samples, which can be difficult or impossible to obtain. Finally, the analyses are
57 lengthy and costly. To complement these destructive measurements therefore, there is
58 considerable interest in developing spectroscopic methods to detect and quantify ^{90}Sr on site.
59 ^{90}Sr is one of the main pure beta emitting radionuclides found in nuclear dismantling sites and
60 given its radiotoxicity, locating and quantifying ^{90}Sr activity is essential to evaluate
61 radiological impact on workers. It is in this context that non-destructive techniques to measure
62 ^{90}Sr activity in contaminated soils were developed by different research laboratories
63 worldwide [1–13].
64 Building on existing methods, the objective of the study reported here was to develop
65 a device for on-site characterization of soils, building structures (e.g. concrete shells) and
66 samples contaminated with ^{90}Sr. More specifically, the project was to develop a dedicated β-
67 spectrometer to detect and quantify ^{90}Sr via its decay product ^{90}Y by rigorously modeling the
68 detector's response and accounting for contribution from ɣ photons and unwanted β- particles.
69 The first part of the article presents the measurement method, the dimensioning studies
70 carried out using the particle transport codes MCNP6 [14] and PENELOPE [15], and the
71 design of the detector with an EJ200 plastic scintillator. The electronics of the device and the
72 spectrometric chain are also described. The second part focusses on the energy and efficiency
73 calibration of the β- spectrometer as well as on the determination of calibration coefficients by
74 numerical simulation for various on-site measurement configurations. This involved
75 comparing the theoretical response calculated using MCNP simulations to experimental
76 measurements obtained using standard β- sources. The third part of the article reports and
77 discusses the results obtained using the device for the quantification of ^{90}Sr activity in

78 samples of Fontainebleau sand from the CEA (French Alternative Energies and Atomic
79 Energy Commission) site at Fontenay-aux-Roses in comparison with radiochemical analyses.

80 2. Materials and methods

81 *2.1. β- spectrum acquisition and interpretation*

82 The measurement technique used here is based on the work of Chesnokov and al. [2]
83 and Potapov and al. [3] to characterize soils contaminated by the Chernobyl nuclear accident.
84 More recently, Slaninka and al. [4] have compared this non destructive method with
85 radiochemical analyses. The principles are outlined here as they underpin the work reported in
86 this article. More detailed descriptions can be found in the original references.

87 *2.1.1. ^{90}Sr decay*

88 Strontium-90 is an unstable nucleus with an excess of neutrons that undergoes
89 spontaneous β-– decay. The parent nucleus decays to ^{90}Y with a half-life of 28.8 years,
90 emitting electrons with a maximum kinetic energy of 0.546 MeV [16]. This intermediate
91 nucleus then decays with a half-life of 64 hours either to an excited state of ^{90}Zr by emitting
92 an electron with a maximum energy of 0.518 MeV (~0.017% probability), or directly to stable
93 ^{90}Zr by emitting an electron with a maximum energy of 2.280 MeV. In the latter case, the β-–
94 radiation emitted is more energetic and therefore more easily detected and measured than the
95 initial emission from ^{90}Sr. Since both nuclides are at secular equilibrium, ^{90}Sr activity can be
96 evaluated through the β- particles emitted by its daughter nucleus, ^{90}Y.

97 *2.1.2. Spectrum acquisition*

98 The nuclear activity of ^{90}Sr can be determined by acquiring two separate spectra with a
99 scintillation detector. For the first, the main measurement, the detector is placed very close (a

few millimeters) from the surface of the studied material so that the β-– and ɣ rays are absorbed by the scintillating material in the detector. This deposition of energy leads to the emission of light photons that are directed through an optical waveguide to a photomultiplier tube. The second or auxiliary spectrum is recorded with an aluminum cover placed between the detector and the sample. This blocks the β- particles but not the ɣ rays emerging from the studied area such that only the latter enter the detector. Subtracting the second spectrum with appropriate processing yields the net β-– signal from which the ^{90}Sr activity can be estimated.

2.1.3. Spectrum processing and interpretation

2.1.3.1. Unwanted signals from other radionuclides

Since ^{90}Sr is a fission product, it is almost always found in nuclear installations with other fission products, notably ^{137}Cs, which undergoes β-– decay to metastable ^{137m}Ba with a half-life of 30,05 years [16]. The other main artificial radionuclide that emits both β- and ɣ rays is ^{60}Co, produced by neutron activation from ^{59}Co in nuclear reactors [16]. Natural radionuclides may also interfere with the measurements. In soil and concrete, the main natural radioisotopes are ^{40}K and those in the ^{238}U, ^{235}U and ^{232}Th series which are all mixed alpha, beta and gamma emitters. According to the IAEA, the concentration ranges of ^{40}K, ^{232}Th and ^{226}Ra in common types of concrete are about 5–1,570 Bq·kg^{-1}, 1–190 Bq·kg^{-1} and 1–250 Bq·kg^{-1}, respectively [17]. Signals from natural radionuclides, are thus only important to consider for low levels of ^{90}Sr contamination, in particular the ^{234m}Pa, a ^{238}U daughter, which emits an electron with a maximum energy of 2.280 MeV [16], i.e. same as ^{90}Y. The clearance level set by the European Commission for building rubble from nuclear installations is of the order of 1000 Bq·kg^{-1} [18]. For walls and floors, the difficulty lies in locating the contamination and identifying its surface or volume within the background contribution from mixed β-/ɣ emitters, retaining only the contribution from ^{90}Sr.

2.1.3.2. Spectrum analysis

To eliminate this background contribution, two key facts are that the components of the β- and ɣ spectra below 0.7 MeV come mainly from ^{137}Cs contamination, while those above 0.7 MeV come from natural radionuclides and ^{60}Co if present. Therefore, the high-energy β-− background in the spectra from natural radionuclides can be estimated by correlating their β-− spectrum with the ɣ component above 0.7 MeV. The number of electrons and photons in the background noise over an energy interval ΔE_γ are correlated as follows [2,3]:

$$N_e = \sigma^* N_\gamma + \Delta\sigma N_\gamma^U \quad (1)$$

with $\sigma^* N_\gamma$ being the correlation between the number of ɣ photons and electrons from the background noise and $\Delta\sigma N_\gamma^U$ the correlation that takes account of natural radioactivity.

2.1.4. Determining ^{90}Sr activity

Once the background contribution has been eliminated, the activity of ^{90}Sr can be calculated using Eq. (2):

$$A_{^{90}\mathrm{Sr}} = \left\{\left[N_{e\gamma}(\Delta E_e) - N_\gamma(\Delta E_e)\right] - \left[\sigma^* N_\gamma\left(\Delta E_\gamma\right) + \Delta\sigma N_\gamma^U\right]\right\} \times C \quad (2)$$

Here, $N_{e\gamma}(\Delta E_e)$ and $N_\gamma(\Delta E_e)$ are the count rates measured respectively without and with the aluminum cover in the energy range ΔE_e, $\left[\sigma^* N_\gamma\left(\Delta E_\gamma\right) + \Delta\sigma N_\gamma^U\right]$ is the count rate from background noise in the same energy domain, and C is a calibration coefficient that converts the measured count rate into ^{90}Sr activity. It is equal to the count rate that would be measured for unit activity of ^{90}Sr/^{90}Y in the studied concrete or soil.

Potapov and al. [3] defined the following energy ranges : ΔE_{e1}= 0.9–2.0 MeV, ΔE_{e2}= 1.2–2.0 MeV and ΔE_γ= 1.09–2.00 MeV. The first interval (ΔE_{e1}, shown in green in Fig. 1) is

designed to minimize statistical uncertaintys in the measured ^{90}Sr activity due to the presence of ^{137}Cs [3]. This was the range used by default in the work reported here. The second interval (ΔE_{e2}), with a lower limit shifted up to 1.2 MeV is more appropriate in the presence of high ^{60}Co concentrations. The ɣ-ray interval (ΔE_{γ}) is designed to minimize background β-radiation noise from natural radionuclides.

2.2. Dedicated detector design

2.2.1. Main β- particle detection techniques

Beta particles can be detected destructively in dissolved samples using a liquid scintillation counter [19]. Another standard approach involves two superposed passivated implanted planar silicon detectors in a vacuum chamber [9]. This is routinely used in α spectrometry and has been developed for environmental matrices to detect and quantify natural and artificial β- emitters [10]. In the same way, Sokolov and al. [11] have developed a SiLi detector inside a vacuum chamber to detect both beta and X-ray radiation from different kind of samples. Howewer, the design of these detection unit severely limits their applicability for in situ measurements. Kadenko and al. have developed a portable β-spectrometer consisting of an activated polystyrene scintillator, a photomultiplier tube, and a multichannel analyzer [12]. The ^{90}Sr activity can be determined from the count rate measured in the region of interest 1311-2282 keV. The US Department of Energy [8] have developed a BetaScint fiber-optic sensor for detecting ^{90}Sr and ^{238}U in soil. It consists of a multi layers of scintillating fiber optic arrays, which affords some discrimination against low energy beta particles, gamma rays and cosmic-rays by measuring coincident events. Due the large area of the BetaScint, the measurements are more representative of the contamination in the soil against laboratory measurements on samples. The main limitation of the BetaScint is that the beta radiation from ^{90}Sr and ^{238}U cannot be discriminated. Finally, the combined scintillators

with different pulse shape characteristics in phoswich (phosphor sandwich) detectors allow low-energy radiation (ɣ, X-ray, α or β-) to be distinguished from the background noise thanks to pulse shape (in particular response time) analysis. Farsoni and Hamby have developed a real-time detector for simultaneous ɣ and β- spectrometry, with three scintillators—a plastic scintillator in front of CaF_2(Eu) and NaI(Tl) crystals—and a customized digital pulse processor [13].

2.2.2. Study design

The objective of this part of the study was to dimension a device able to provide analyzable β- spectra to estimate ^{90}Sr activity in the studied object (concrete structure, contaminated sample, filter, etc.), by characterizing the source term, choosing the detector, and designing the aluminum cover. For the source term, the task was to predict the paths and energy distribution of electrons emerging from concrete structures contaminated with ^{90}Sr and potentially interacting with the detector. This involved calculating the path length of electrons emitted by ^{90}Y in various concrete matrices of different densities in comparison with previously published results for contaminated soils [2,3]. Choosing an appropriate detector is crucial as it governs the measurement performance of the detector. The main criteria considered were the detection efficiency, sensitivity to ɣ rays, and the electron backscattering coefficient. Several materials were considered and electron and ɣ responses of two plastic scintillators, the BC400 (Saint-Gobain, France) and EJ200 (Eljen Technology, TX, USA), were compared using Monte-Carlo simulations. Finally, the design and dimensions of the aluminum cover used to block electrons during the auxiliary measurement were optimized. The influence on incident β-– radiation of the window protecting the scintillator from ambient light and humidity (the material is hygroscopic) was quantified and minimized. Simulations were performed mainly with MCNP6 [14] and validated using PENELOPE [15].

2.2.3. Electron path length in soil and concrete contaminated with ^{90}Sr

To estimate the maximum measurable depth of ^{90}Sr contaminations, electron paths through various soil or concrete shells were modeled using MCNP6 simulations. A surface source of β-− radiation (10 × 10 cm²) was placed under layers of non-contaminated material (soil or concrete) with different thicknesses. The β-− particles were emitted vertically with an energy distribution corresponding to those emitted by ^{90}Y (E_{max} = 2.280 MeV). An F1 surface current tally was performed on the upper surface of the uncontaminated matrix, giving the number of electrons that pass through the matrix layer. Fig. 2 shows that the proportion τ of electrons generated by the source that penetrate through the layer depends on its thickness and density. Above 5 mm of concrete and 7 mm of soil, the proportion of electrons passing through the layer becomes negligible. These results of simulation were confirmed by calculating the range of electrons with an energy Q_β= 2.280 MeV (the maximum energy of electrons emitted by ^{90}Y) using the Flammersfeld equation [20] which gives respective path lengths of 0.71 and 0.47 cm in soil (1.52 g·cm^{-3}) and concrete (2.3 g·cm^{-3}).

2.2.4. Components and dimensions of the β-− spectrometer

2.2.4.1. Active part of the detector

Plastic scintillators like BC400 (Saint-Gobain, France) or EJ200 (Eljen Technology, TX, USA), both based on polyvinyltoluene, are well adapted for the detection of electrons [21,22]. Indeed, since they are composed mainly of carbon and hydrogen, they have a low mean atomic number, meaning that very few incident electrons are scattered, ɣ photons do not deposit much energy, and bremsstrahlung is negligible.

2.2.4.2. Optimal plastic scintillator thickness

Electron interactions in the plastic scintillator were simulated using MCNP6 and PENELOPE to calculate the energy deposited in the detector as a function of its thickness. The model consisted of a square 10 × 10 cm² concrete slab, 0.5 cm thick (the maximum range of β-− particles from ^{90}Y), with different thicknesses of scintillating plastic placed on top, separated by a 1 mm thick layer of air. The ^{90}Y source term was homogeneously distributed in the concrete. Fig. 3 shows how the energy deposited varies as a function of the thickness of the scintillator as estimated using an F8 tally with MCNP6. The results with EJ200 and BC400 are almost identical because their compositions are similar. The energy deposited in the scintillator increases before leveling out at a thickness of about 10 mm, which corresponds to the path length of β-− particles with an energy of 2.280 MeV in the scintillator material [20]. However, since 95% of the energy is deposited in the first 4 mm, this thickness was chosen as a good compromise between maximizing the detection efficiency of β- particles from ^{90}Y and minimizing the sensitivity to gamma photons.

2.2.4.3. Optimal window design

The window acts as a protective film, limiting interference from ambient light and preventing direct contact between the sensitive part of the detector and the studied material. It must nonetheless be thin and as transparent as possible to electrons. To limit electron energy loss on entering the device, we investigated the effects of a 18 µm Mylar film as a potential improvement on the 50 µm titanium sheet used in the device developed in references [2,3]. Mylar (biaxially oriented polyethylene terephthalate) is a polyester film commonly used to protect scintillation detectors. We performed MCNP6 simulations with a cylindrical detector (⌀ = 8 cm) and a 5 mm thick cylindrical layer of concrete emitting β-− particles with the energy distribution of ^{90}Sr/^{90}Y electrons. Fig. 3 shows that Mylar is more transparent to

electrons than titanium, absorbing about 10 keV less energy at the same thickness. As expected furthermore, the most transparent film is the thinnest, so the best choice is a Mylar film with a thickness of 18 µm which also enable the detector to be light-tight.

2.2.4.4. Optimal aluminum cover thickness

As mentioned above, aluminum shielding is required to take auxiliary readings of the background ɣ radiation. The low atomic number of aluminum is advantageous for this purpose as it interacts weakly with ɣ photons, with little bremsstrahlung, while being effective at stopping electrons. According to Flammersfeld equation [20], the path length of β-– particles with an energy of 2.280 MeV in aluminum (2.698 $g \cdot cm^{-3}$) is 0.408 cm. A 4 mm thick sheet of aluminum should therefore stop all the electrons emitted by ^{90}Y. To verify this, the simulations reported in the previous section were repeated with aluminum layers of different thicknesses inserted between the concrete and the Mylar film. The results obtained with MCNP6 and PENELOPE, compared in Fig. 4, are very close. The energy deposited in the detector decreases from about 60 keV without the shield (Fig. 3) to 1 keV with a 2 mm thick shield and becomes negligible for thicknesses of 4 mm and above (Fig. 4). A thickness of 4 mm was therefore chosen for the aluminum cover used in practice.

2.2.4.5. Optimal β-– spectrometer design

The detector used in the rest of the study was custom-built by the manufacturer Scionix (Bunnik, The Netherlands) using the results of the dimensioning studies described above. The device consists of a 4 mm thick EJ200 plastic scintillator with an 18 µm thick Mylar window. The scintillator is attached to a PMMA light guide that directs the photons to the photocathode of a photomultiplier. The detector was attached via a DSA1000 multichannel analyzer (MIRION Technologies, CA, USA) to a computer running the software

Génie 2000 [24], which was used to calibrate the device and acquire and analyze the spectra (Fig. 5).

3. Calibration and characterization of the EJ200 detector's response

The next stage of the study was to build a numerical model of the detector with MCNP6 and validate it using spectra measured using calibration sources in controlled setups, minimizing the relative error between simulated and measured spectra. After qualifying the model, Monte Carlo simulations were performed to determine the calibration coefficient *C* in Eq. (2) for different measurement setups likely to be encountered in the field.

3.1. Experimental measurements using calibration sources

The reference spectra were measured using surface calibration sources, mainly pure β-emitters (^{14}C, ^{36}Cl, ^{90}Sr/^{90}Y and ^{204}Tl) and a mixed β-/ɣ emitter (^{137}Cs). The dynamic range of the spectrometer was calibrated beforehand using a ^{90}Sr/^{90}Y source placed up against the detector, to limit losses in air. The gain of the device was thus adjusted so that the β-– spectrum of ^{90}Y would cover all the 1024 channels of the 10 bits dynamic range.

The characteristics of the sources are summarized in Table 1. Their radioactivity was measured at the time of the measurements, namely on 23 June 2015. The ^{36}Cl, ^{90}Sr/^{90}Y, ^{204}Tl and ^{137}Cs sources consisted of a 30 mm diameter active layer obtained by evaporating a solution between two 75 µm thick gold-coated plastic sheets held by a 3 mm thick metal ring [25]. The ^{14}C source had a 51 mm diameter thick active layer, obtained by evaporating a solution deposited on an aluminum sheet, covered by a protective layer [25].

The detector was placed at a fixed distance (as close as possible) vertically above each source. To prevent direct contact with the fragile Mylar window, the detector was placed on two 8.5 mm spacers, leaving 9.65 mm of air between the detector and the source. With the

283 ^{137}Cs source, a mixed β-/ɣ emitter, auxiliary measurements were taken with the aluminum
284 cover to obtain the β- contribution alone after subtraction. The acquisition time for each
285 spectrum was 10 min to ensure good counting statistics.

286 ## *3.2. Numerical model of the detector*

287 The method described above for the measurement of ^{90}Sr activity in concrete and soil
288 involves calculating calibration coefficients from Monte Carlo simulations of various
289 measurement setups. The reliability of these simulations depends in turn on the reliability of
290 the numerical model of the detector. The following section describes how the model of the
291 EJ200 detector was built and validated using MCNP6 simulations and the reference spectra.

292 ### *3.2.1. Modeling the EJ200 detector using MCNP6*

293 The model was built using data provided by Scionix on the nature and dimensions of
294 the different components and by LEA (Pierrelatte, France) on the characteristics of the
295 calibration sources. Since the path length of the electrons is short, the parts of the detector
296 beyond the light guide have little effect on the measurements and were therefore not included.
297 The composition and density of the materials in the model were taken from the Pacific
298 Northwest National Laboratory database [26]. The surface-like radioactive source was
299 modeled as a very thin cylinder of air with a diameter specified by the manufacturer [25] and
300 a uniformly distributed activity. The characteristic β- spectra of each of the radionuclides
301 were modeled by emission probabilities in energy intervals obtained from the Joint Evaluated
302 Fission and Fusion radiological database [27]. A 5 keV energy step was used and continuous
303 spectra were obtained by interpolation using MCNP6.
304 Several features of the radioactive decays were not included in the model. First, for
305 mixed β-/ɣ emitters such as ^{137}Cs, the electron spectrum also contains a separate component
306 from the internal conversion process, which occurs in competition with gamma emission.

There is also an internal conversion component in the electron spectrum of ^{90}Y, but it is too weak to be included in the model. The emission of internal conversion electrons is followed by a reorganization of the electron shell and the emission of X-rays; this process was ignored in the Monte Carlo simulations. Second, for mixed β-/ɣ emitters, the source of ɣ rays was not included in the calculations because the corresponding contributions to the spectra are subtracted from the experimental data using the auxiliary spectrum but not necessarily all their beta components. Third, ^{36}Cl and ^{204}Tl decay by electron capture followed by the emission of ɣ photons if the daughter nucleus is in an excited state, and by the emission of X-rays and Auger electrons as the electron shell reorganizes. Because of the complexity of the source term corresponding to this decay process, it was not included in the Monte Carlo simulations.

Fig. 6 shows a cross-section of the setup used for MCNP6 simulations with a ^{137}Cs source. An F8 tally was used to calculate the distribution of electron energy in the sensitive part of the detector (representing the EJ200 plastic scintillator). The PE (photon and electron transport) mode was used to account for the transport of secondary electrons produced by bremsstrahlung radiation and fluorescence X-rays in the material down to a minimum particle energy of 1 keV (the default setting in MCNP6 [6]). Electron transport was modeled using the ITS (Integrated TIGER series) algorithm [28], as an add-on to the code, which results suggest is more accurate that the default MCNP algorithm [29–31]. To ensure meaningful comparisons between the experimental and simulated spectra, the detector was energy calibrated using the same intervals as used for the F8 tally in MCNP6.

3.2.2. Energy calibration of the detector

Energy calibration involves linking each of the detector's channels to an energy. To increase the precision of the calibration, several {energy; channel} pairings are typically used, covering the whole dynamic range. Monoenergetic electrons such as those emitted along with

ɣ rays in internal conversion processes are well suited for this process. In the present work, the detector was energy calibrated using ^{137}Cs and ^{14}C sources.

The electron spectrum of ^{137}Cs has characteristic internal conversion peaks at 0.624 and 0.656 MeV [27], which were used to define a first {energy; channel} pair. A second pair was obtained from the beta emissions of ^{14}C, whose spectral density is concentrated at low energies (maximum energy, 0.156 MeV) and is therefore well suited to calibrate the channel with the highest counting rate. Note that since the two energy ranges required to calculate ^{90}Sr activities in this approach (Eq. (2)) are quite broad (ΔE_{e1}= 0.9–2.0 MeV or ΔE_{e2}= 1.2–2.0 MeV), a rough calibration of the spectrometer using just two {channel; energy} pairs, respectively at low and medium energies, was considered adequate.

Monte Carlo simulations were used to estimate the energy loss of electrons emitted by the two sources in the air-filled gap separating them from the detector. These simulations yielded the energies corresponding to the maximum counts for the ^{14}C spectrum in channel 18 and the internal conversion peak of the ^{137}Cs spectrum in channel 240. For the simulated ^{14}C spectrum, the count rate maximum occurred at 0.049 MeV.

The internal conversion electrons emitted by ^{137m}Ba have energies of 0.624 or 0.656 MeV and respective intensities of 8.07 and 1.50% [27]. The beta spectrum of ^{137}Cs should therefore contain two peaks, but only one was observed experimentally, indicating that the energy resolution of the detector is lower than the separation of the two lines. As a first approach, we assumed that the main component of the measured peak was the more intense line at 0.624 MeV. A Monte Carlo simulation was performed without taking the resolution of the detector into account. Fig. 7 shows the energy distribution in the scintillator from the two types of internal conversion electrons (orange line). The maximum count rate occurs at 0.604 MeV, indicating that the electrons lose about 20 keV in passing through the layer of air and the Mylar film.

The energy calibration equation deduced from the two calibration points, {channel 18; 0.049 MeV} and {channel 240; 0.604 MeV}, obtained from the experimental and simulated ^{14}C and ^{137}Cs spectra is thus:

$$E(MeV) = 0.0025 \times \text{channel} + 0.004 \quad (3)$$

3.2.3. Energy resolution parameters

In MCNP6 simulations, the detector is assumed to be ideal and the different sources of dispersion of charges are ignored. However, the finite resolution of the detector can be taken into account in the code (using the Gaussian energy broadening ("GEB") option in the input file) via the following function that gives the resolution of the detector (the full width at half maximum (FWHM) of the peaks) as a function of energy (E) [14]:

$$\text{FWHM} = a + \sqrt{b(E + cE^2)} \quad (4)$$

The coefficients a, b and c were determined using the experimental data measured for ^{137}Cs. The experimental data were fitted [32] using a Gaussian function. The FWHM of the peak is about 30 channels, or 0.075 MeV according to the energy calibration equation (Eq. (3)), this means that the energy resolution of the detector is about 12.5%.

The three coefficients in Eq. (4) were then determined using three {FWHM; E} pairs, the first at the origin {0 MeV; 0 MeV}, the other two corresponding to the two internal conversion peaks {FWHM = 0.078 MeV; E = 0.624 MeV} and {FWHM = 0.082 MeV; E = 0.656 MeV}. Fitting Eq. (4) to these three data points then gives a = 5.272×10^{-6} , b = 6.718 $\times 10^{-2}$ and c = 1.901.

The spectra simulated with and without this finite detector resolution are compared in Fig. 7. The maxima of both spectra appear at 0.604 MeV, therefore in the same channel, and

the energy corresponds to that of the maximum count rate for the most intense internal conversion peak. This comparison thus confirms the hypothesis that the dominant contribution to the experimental peak measured for ^{137}Cs is from electrons emitted at 0.624 MeV, and also validates the energy calibration equation (Eq. (3)) obtained without accounting for the energy resolution of the detector.

3.2.4. MCNP6 model qualification

Simulations of the electron energy distribution in the plastic scintillator were performed using MCNP6 for all the calibration sources (^{14}C, ^{36}Cl, ^{90}Sr/^{90}Y, ^{137}Cs and ^{204}Tl), integrating energy intervals and detector resolution as described above. Figs. 8–10 respectively compare the measured and simulated spectra of ^{14}C, ^{90}Sr/^{90}Y and ^{137}Cs. The simulated spectra reproduce the main features of the experimental spectra. The maxima occur at the same energies and the high-energy tails of the simulated and experimental spectra overlap, tending to zero at the same energies. These results indicate that the energy calibration of the device is accurate over the whole measurement range.

The spectra were compared quantitatively in terms of integrated count rates for different energy intervals. For ^{14}C, ^{36}Cl and ^{204}Tl, the count rates were integrated over the entire measurement range, namely 0.031–0.156 MeV for ^{14}C, 0.031–0.709 MeV for ^{36}Cl and 0.031–0.763 keV for ^{204}Tl. For ^{137}Cs, the energy interval (0.508–0.700 MeV) was defined to only consider the internal conversion peak. For ^{90}Sr/^{90}Y finally, the count rates were integrated over the two energy ranges defined previously, ΔE_{e1}= 0.9–2 MeV and ΔE_{e2}= 1.2–2 MeV.

The relative deviations between the simulated and measured count rates over these energy ranges are listed in Table 2. The simulated spectra tend to underestimate the count rates between 0.03 and 0.7 MeV with a maximum relative deviation of 29%, and overestimate those between 0.7 and 2.2 MeV with a maximum relative deviation of 33%. There are several

possible sources of uncertainty in this context: (i) uncertainties from approximating certain calibration sources (^{137}Cs, ^{204}Tl and ^{36}Cl) as pure β-– emitters (see section 3.2.1), (ii) uncertainties from the electron transport model—the transport algorithm used, uncertainties in the nuclear data, in particular the effective interaction cross-sections, and the cut-off used for electron and photon transport (1 keV, the default value), and (iii) uncertainties in the setup geometry—in the thicknesses of the different layers and in the assumed uniformity of the source term distribution.

Because of the multiple sources of uncertainty, a sensitivity analysis was carried out, focusing on the most easily quantified uncertainties, namely the transport algorithm and the modeling of the source term. There are three possible choices for the electron transport algorithm in MNCP6 [14]: ITS, the one used for the above simulations; “mncp”, the default option in MCNPX; and “Landau”, the default option in MCNP6. To quantify the uncertainty from the choice of algorithm, the simulations with the ^{90}Sr/^{90}Y source were repeated using the mncp and then the Laudau transport algorithms (data not shown). For the latter, the energy cut-off for electron and photon transport had to be decreased to 20 eV instead of the 1 keV defined by default in MCNP6 [14]. Using the mcnp algorithm reduces the relative deviation between simulated and experimental spectra by a few percentage points in the interval 0.9–2 MeV and by a few tens of percentage points in the 1.2–2 MeV region. Using the Landau algorithm did not reduce the relative deviation from the experimental data, except for energies below 0.7 MeV, and the lower electron transport cut-off significantly increased the simulation times.

The second source of uncertainty investigated was the modeling of the source term, assumed to be uniformly distributed. To investigate the effect of a non-uniform source distribution, simulations were carried out with ^{90}Sr/^{90}Y sources arranged in a regular pattern of circular deposits on the substrate (data not shown). The results obtained differed little from

427 those with a uniformly distribute source, showing that this assumption has little influence on
428 the simulated spectra and cannot explain the observed deviations from the experimental data.
429 The conclusion of this sensitivity analysis is that the observed differences between the
430 observed and simulated spectra cannot be explained by a single source of uncertainty but are
431 likely due to a combination of the multiple identified sources of uncertainty. The MCNP
432 model of the detector can be considered qualified based on these results, with a maximum
433 relative deviation of 30% from the experimental data. This upper estimate was used thereafter
434 as the conservative relative uncertainty of the Monte Carlo simulations.

435 ## *3.3. Calibration coefficients*

436 The method adopted here to estimate the ^{90}Sr activity of contaminated soils rests on
437 Monte Carlo simulations of different measurement setups to establish calibration coefficients
438 (*C* in Eq. (2)) [2,3].

439 ### *3.3.1. ^{90}Sr-contaminated concrete*

440 The method, which was initially developed to study ^{90}Sr-contaminated soils, was first
441 applied here to concrete structures contaminated with ^{90}Sr. Sensitivity analyses were carried
442 out to determine the variation of the calibration coefficient as a function of the diameter of a
443 surface source and its depth in the substrate. As a first approach, the horizontal and vertical
444 distributions of the contaminant were both considered uniform.

445 #### *3.3.1.1. Sensitivity analysis in terms of the surface area of the contamination*

446 The calibration coefficient in Eq. (2) was calculated for surface sources ranging from
447 6–156 mm in diameter in 10 mm steps. The source was modeled as a cylinder with a height of
448 0.1 mm made of air with a uniformly distributed activity of 1 Bq·cm^{-2}. The concrete was
449 assumed to have a standard composition [26] and a density of 2.3 g·cm^{-3}. Calculations were

450 performed with the detector either in direct contact with the source, to optimize the β-
451 detection efficiency, or at distance of 4 mm (corresponding to the thickness of the aluminum
452 cover), to evaluate the effect of the detector's positioning with respect to the ground.
453 Fig. 11 shows how the calibration coefficient for the energy range 0.9–2.0 MeV varies
454 as a function of the diameter of the source in these two arrangements. When the detector is in
455 direct contact with the ground, the calibration coefficient plateaus at diameters above 76 mm.
456 This is because the electrons from the outer parts of the source are stopped by the aluminum
457 casing when the source becomes wider than the scintillator. The detection efficiency is lower
458 when the detector is placed 4 mm from the concrete floor. The difference is about 20% at a
459 source diameter of 76 mm. However, the calibration coefficient levels out more gradually,
460 tending towards the value in direct contact for sources wider than 130 mm. Similar data were
461 obtained for the other energy interval of interest (1.2–2.0 MeV, data not shown). These results
462 indicate that measurements in direct contact with the contaminated surface are more efficient
463 than at a distance when the contaminated area is no larger in diameter than the scintillator (76
464 mm). The calibration coefficients calculated in this configuration for a uniform surface
465 contamination are listed in Table 3.

466 *3.3.1.2. Sensitivity analysis in terms of the depth of the source*

467 The same approach was used to evaluate the effect of the depth of the source. A
468 cylinder of air 76 mm in diameter with a uniformly distributed volume activity of 1 $Bq \cdot cm^{-3}$
469 was placed at a depth of 0.5–6 mm in the concrete floor. The concrete was modeled as before
470 and the detector was placed in direct contact with the floor.
471 The variation of the calibration coefficient with the depth of the source is shown in
472 Fig. 12 for both energy intervals. The profiles are similar, an increase followed by a plateau,
473 but the maximum occurs at a depth of about 3 mm for the energy interval 0.9–2.0 MeV versus
474 about 2 mm for electrons in the energy range 1.2–2.0 MeV. This is expected because the

electron spectrum shifts to lower energies as the depth of the source increases and the electrons lose more energy passing through the concrete. This means that electrons with energies greater than 0.9 MeV do not contribute to the detector's response in the 0.9–2.0 MeV interval if the source is covered by more than 3 mm of concrete. For electrons with an energy greater than 1.2 MeV (the 1.2–2.0 MeV interval), the corresponding threshold is 2 mm. The calibration coefficients determined under these conditions are listed in Table 3.

If the contamination is uniformly distributed down to a depth of more than a few millimeters, the mass activity can be deduced from the measurements obtained for the first few millimeters of contaminated concrete using the calibration coefficients in Table 3. The difficulty then lies in defining the minimum depth at which this conversion is valid. For surface or volume contaminations in the first few millimeters of concrete indeed, the mass activities obtained from the calibration coefficients will substantially underestimate the true values. These uncertainties are specific to substrates in which ^{90}Sr is liable to migrate (soils, concrete, etc.). For surface-contaminated industrial waste, the use of surface calibration coefficients provide close overestimates of the true activity.

3.3.1.3. Estimated setup-specific detection limits

The detection limit corresponds to the situation in which the signal from contaminated concrete is the same as the background signal from non-contaminated concrete [33].

The background β- spectrum from radionuclides naturally present in concrete (^{40}K and the daughter nuclei of ^{238}U and ^{232}Th) was obtained by taking the difference of the spectra measured over 16 h with and without the aluminum cover in direct contact with a non-contaminated concrete floor (Fig. 13). The count rates were then calculated in the two energy intervals of interest, 0.9–1.2 and 1.2–2.0 MeV.

The detection limits of the system were calculated for different on-site measurement times (10, 20, 30 and 60 min for each spectrum with and without the aluminum cover) and

500 then converted to mass activities using the calibration coefficient (Table 3) calculated for
501 concrete with a uniform contamination of ^{90}Sr down to a depth of 3 mm. The values obtained
502 are listed in Table 4.

503 *3.3.2. ^{90}Sr-contaminated Fontainebleau sand*

504 In view of applying this method to various types of soil encountered in
505 decommissioning sites, measurements were performed on samples of Fontainebleau sand
506 from the CEA (French Alternative Energies and Atomic Energy Commission) site at
507 Fontenay-aux-Roses. Furthermore, to assess the possibility of analyzing multiple samples
508 using an autosampler, measurements were also taken on sand samples conditioned in
509 standardized 500 cm^3 polyethylene (SG500) containers, which are mainly used to analyze
510 liquid samples by gamma spectrometry.

511 *3.3.2.1. Direct measurements on bare sand*

512 The variation of the calibration coefficient in Eq. (2) with the depth of a volume
513 source was calculated as described above (section 3.3.1.2) with the concrete replaced by
514 Fontainebleau sand. As before, the detector was placed in direct contact with the substrate to
515 maximize the detection efficiency. The composition of the sand was assumed to be 100%
516 SiO_2, with a density of 1.5 $g \cdot cm^{-3}$ [34].
517 The depth profiles obtained for the two energy ranges of interest are shown in Fig. 14.
518 The trends are the same as those observed for contaminated concrete (cf. Fig. 12). However,
519 since sand is less dense than concrete, the electrons travel further and the maximum count rate
520 occurs at a depth of 4.5 mm (rather than 3 mm for concrete). The corresponding calibration
521 coefficients are listed in Table 3. The calibration coefficients for surface contamination are
522 similar to those obtained for concrete (Table 3). The nature of the substrate therefore has little
523 effect on electron transport, particularly in terms of backscattering from the surface.

3.3.2.2. Measurements on sand in SG500 containers

The aim of these measurements was to evaluate the sensitivity loss due to the polyethylene container. Fig. 15 shows the setup used for the Monte Carlo simulations, with the SG500 container placed centrally and directly against the aluminum frame of the detector. The container was modeled as realistically as possible, with two separate compartments and a wall density (0.939 $g \cdot cm^{-3}$) corresponding to the mean of the reference values for low- and high-density polyethylene (respectively 0.917–0.930 $g \cdot cm^{-3}$ [35] and 0.944–0.965 $g \cdot cm^{-3}$ [36]). The decrease in signal intensity due to the container was assessed by simulating the $^{90}Sr/^{90}Y$ spectra of uniformly contaminated Fontainbleau sand in a SG500-type container with either air or polyethylene walls (Fig. 16). Compared with direct measurements on bare sand, the count rates with an SG500 container are approximately 8 and 16 times lower in the 0.9–2.0 MeV and 1.2–2.0 MeV regions, respectively (Table 3). One possibility to increase the detection efficiency if ^{137}Cs is present but not ^{60}Co would be to extend the measurement range to lower energies (down to 0.3 instead of 0.9 MeV). In this configuration indeed, the beta spectrum of ^{137}Cs is shifted to energies below 0.3 MeV. Samples co-contaminated with ^{60}Co have not been studied so far.

4. Results for samples of contaminated Fontainebleau sand

To validate this method for quantifying ^{90}Sr activity, measurements were performed on 10 samples of contaminated sand from the CEA decommissioning site at Fontenay-aux-Roses. Previous laboratory-based radiochemical analyzes revealed that the main radionuclides in the samples were ^{238}Pu, ^{237}Np, ^{233}Pa, ^{90}Sr, with ^{137}Cs and $^{239}Pu+^{240}Pu$ also present in some samples (Table 5). The main reasons for choosing these samples were that the main emitter is ^{90}Sr, that the mass activity of ^{90}Sr varies from a few to a few hundred $Bq \cdot g^{-1}$, and that some of samples contain ^{137}Cs. Note that while some of the daughter nuclei in the decay chain of

548 ^{239}Pu, ^{238}Pu, ^{237}Np and ^{233}Pa emit β- particles with energies similar to those of ^{90}Y, these
549 contributions were considered negligible because the activity of these radionuclides in the
550 samples is two decades much lower than that of ^{90}Sr.

551 Two measurement setups were used, as described in section 3.3.2 and shown in Fig.
552 17; the detector was placed either in direct contact with the sand (for all ten samples), or with
553 the sample in a SG500 container placed on top of the detector (for four samples). Since the
554 samples had been stored in SG500 containers, the direct measurements involved spreading
555 some of their contents in a larger diameter container. To avoid contaminating the detector, a
556 layer of Parafilm M® (Bemis, Neenah, WI) was placed between the sand and the detector and
557 between the detector and the SG500 container. Parafilm M is a blend of paraffin and
558 polyolefin on a sheet of glassine paper. The manufacturer lists its thickness as 127 µm and its
559 density as 0.922 g·cm^{-3}.

560 Two acquisition times (for the primary and auxiliary spectra) to obtain good counting
561 statistics in the region of interest (0.9–2.0 MeV) varied from 5 min for the most highly
562 contaminated samples (^{90}Sr activities of hundreds of Bq·g^{-1}) to 20 min for the least
563 contaminated ones (^{90}Sr activities of just a few Bq·g^{-1}). The auxiliary measurements showed
564 that the gamma emissions from the samples in the region of interest were very weak (Fig. 18).

565 Assuming negligible natural radioactivity, the ^{90}Sr activity of the studied samples can
566 be estimated by multiplying the count rate measured in the energy interval of interest,
567 $N_e(\Delta E_e)$, by the calibration coefficient determined using Monte Carlo simulations:

$$A_{\mathrm{Sr}} = N_e(\Delta E_e) \times C \quad (5)$$

568 The calibration coefficients for the two measurement setups were determined (section
569 3.3.2) for a unit activity of ^{90}Sr uniformly distributed in pure SiO_2 with a density of 1.5
570 g·cm^{-3}. The assumption that the ^{90}Sr is uniformly distributed in the samples is reasonable

given the small size of the samples with respect to the extent of the contamination and their granular nature, which favors mixing. Nonetheless, to minimize uncertainties in the measured activities due to uncertainties in the calibration coefficients, another set of more precise simulations was performed, including the layer of Parafilm M and using the measured density of the sand (1.4 ± 0.2 g·cm^{-3}) instead of the previous estimate (1.5 g·cm^{-3}). The additional layer between the detector and the sample shifts the beta spectrum to lower energies and thus reduces the calibration coefficients in the energy regions of interest (Table 3). For the measurements on bare sand, since the calibration coefficient varies with depth down to 4.5 mm (Fig. 14), a sufficiently thick layer of each sample (> 4.5 mm) was poured to ensure the validity of the maximum calibration coefficient. The calibration coefficients obtained for the two measurement setups are presented in Table 3.

The uncertainty in the calibration coefficient was estimated by combining the individual estimates of the uncertainties in the parameters in the model. For the measurements on bare sand, the main sources of uncertainty are the uncertainties in the calibration coefficient (± 30%), in the densities of the sand (± 0.2 g·cm^{-3}) and of Parafilm M (± 10%), and in the position of the source with respect to the detector (± 0.5 mm). For the measurements on sand in SG500 containers, there is an additional contribution from the density of the polyethylene walls, which falls somewhere in the range 0.917–0.965 g·cm^{-3}. These uncertainties (type B) were assumed to be independent and the overall relative uncertainty in the calibration coefficient was obtained by combining the relative values quadratically. The uncertainty range was then doubled to obtain the 95% confidence interval.

The ^{90}Sr activities calculated using Eq. (5) are compared with the values measured by destructive radiochemical analysis in Table 6, corrected for the decrease in ^{90}Sr activity that occurred between the laboratory measurements (in 2013 and 2015) and those with the portable β- spectrometer (in 2016). The values obtained by beta spectrometry on bare sand

tend to be lower than the activities measured by radiochemical analysis, with a maximum relative deviation of 52.9%, while the measurements on sand in SG500 containers tend to be overestimates, with a maximum relative deviation of 57% (Table 6). These deviations can be attributed to uncertainties in the geometry of two models and in the Monte Carlo simulations. The activities measured by beta spectrometry are nonetheless within the estimated uncertainty range of the values obtained by destructive analysis. These results are therefore promising for the use of the portable β- spectrometer on decommissioning sites as a simple, fast and at least semi-quantitative method to characterize difficult to detect radionuclides such as ^{90}Sr.

5. Conclusion

Portable β- spectrometry for the non-destructive detection and quantification of ^{90}Sr is a relatively new research topic at the CEA, motivated by the need for on-site characterization methods for pure β-– emitters. These radionuclides are indeed difficult to detect using classical non-destructive techniques such as gamma spectrometry and are usually quantified by liquid scintillation in the laboratory. The overall aim of the work presented here is to optimize the decommissioning process, namely to improve radioactive waste management and radioprotection measures by providing better information more rapidly on sources, and to minimize costs by optimizing sampling schemes in terms of the number and location of samples analyzed.

Building on a method developed to study soils contaminated by the Chernobyl accident, we updated, adapted and qualified the different components using Monte Carlo simulations before using the system to measure the ^{90}Sr activity of sand samples from a CEA decommissioning site. The results are encouraging and indicate that this simple approach can in the future be used on site to obtain semi-quantitative information on radionuclides that typically require laboratory analyses to detect.

The aim of non-destructive measurement techniques is to complement rather that replace destructive analyses, which will always provide the most accurate quantitative data for decommissioning operations. However, the value of destructive measurements depends on the number and representativity of the samples extracted from the site. The advantage of portable non-destructive techniques is that they can be used directly, on site and on unaltered structures, to identify the spatial distribution (uniform or with hot spots) of the contamination and thus optimize the sampling scheme and the representativity of the samples for laboratory analysis. On site measurements thus improve the sampling and the overall efficiency of the analytical process.

Acknowledgments

The authors would like to thank the team of Analytical Support to Facilities Laboratory (LASE) at CEA Saclay for the provision of standards sources during the step of numerical model validation.

References

[1] C. Cosma, Strontium-90 measurement after the Chernobyl accident in Romanian samples without chemical separation, Spectrochim. Acta B 55 (2000) 1163–1169.

[2] A.V. Chesnokov, S.M. Ignatov, V.I. Liksonov, V.N. Potapov, S.B. Shcherbak, L.I. Urutskoev, M.V. Ivanitskaya, A method for measuring in situ a specific soil activity of 90Sr, Nucl. Instrum. Methods Phys. Res. A 443 (2000) 197–200.

[3] V.N. Potapov, A.G. Volkovich, O.P. Ivanov, V.E. Stepanov, S.V. Smirnov, V.G. Volkov, Development of Portable Beta Spectrometer for Sr-90 Activity Measurements in

641 Field Conditions and its Application in Rehabilitation Activities at RRC Kurchatov Institute,
642 in: Proceedings of the 2006 Waste Management Symposium.
643 [4] A. Slaninka, S. Dulanská, O. Slávik, and Ľ. Mátel, A comparison of 90Sr
644 determination methods using separation on AnaLig® Sr-01 gel and non-destructive direct
645 beta spectrometry, Radiat. Phys. Chem. 112 (2015) 56–60.
646 [5] K H Abel, A J Schilk, D P Brown, M A Knopf, R C Thompson, R W Perkins,
647 Characterization and calibration of a large area beta scintillation detector for determination of
648 Sr90. J Radioanal Nucl Chem 193(1), 99-106, 1995.
649 [6] A J Schilk, K H Abel, D P Brown, R C Thompson, M A Knopf, C W Hubbard,
650 Selective, high-energy beta scintillation sensor for real-time, in situ characterization of
651 uranium-238 and strontium-90. J Radioanal Nucl Chem 193 (1), 107-111, 1995.
652 [7] P D Kalb, L Luckett, D Watters, C Gogolak, L Milian, Deployment of in situ
653 measurement techniques and the MARSSIM process for characterization of the Brookhaven
654 Graphite Research Reactor, BNL-67695.
655 [8] U.S. DOE. BetaScint Fiber-optic sensor for detecting strontium-90 and uranium-238
656 in soil, Innovative Technology Summary Report, OST #70, U.S. Department of Energy
657 Office of Environmental Management, Office of Science and Technology, December 1998.
658 [9] A. Courti, F. Goutelard, P. Burger, E. Blotin, Development of a β- spectrometer using
659 PIPS technology, Appl. Radiat. Isot. 53 (2000) 101–108.
660 [10] P. Bouisset, R. Gurriaran, E. Yerebakanian, and A. Courti, Spectrométrie bêta
661 appliquée aux mesures de la radioactivité dans l'environnement, Radioprotection, vol. 40
662 (2005) 29–45.
663 [11] A.D. Sokolov, A.B. Pchelintsev, A.V. Loupilov, V.A. Zalinkevich, A. Lapenas, Beta
664 and X-Ray Spectrometer for Monitoring of Beta-Radiating Nuclides, IEEE Trans. Nucl. Sci.,
665 50 (2003) 238–240.

[12] I. Kadenko, V. Maydanyuk, V. Petryshyn, G. Primenko, Y. Sedov, Scintillation β-spectrometer with enhanced sensitivity, Appl. Radiat. Isot. 62 (2005) 775–777.

[13] A.T. Farsoni, D.M. Hamby, A system for simultaneous beta and gamma spectrometry, Nucl. Instrum. Methods Phys. Res. A 578 (2007) 528–536.

[14] T. Goorley, M. James, T. Booth, F. Brown, J. Bull, L.J. Cox, J. Durkee, J. Elson, M. Fensin, R.A. Forster, J. Hendricks, Initial MCNP6 Release Overview, Nucl. Technol. 180 (2012) 298–315.

[15] F. Salvat, J.-M. Fernandez-Varea, E. Acosta, J. Sempau, The physics of electron/positron transport in PENELOPE. in: Proceedings of the Ninth EGS4 Users' Meeting in Japan (2001) 1–5.

[16] LNHB, Nucleide Lara, Library for gamma and alpha emissions, http://www.nucleide.org/Laraweb/index.php

[17] International Atomic Energy Agency, Extent of environmental contamination by naturally occurring radioactive material (norm) and technological options for mitigation, in: IAEA Technical Report Series 419 (2003).

[18] European Commission, Recommendations of the group of experts set up under the terms of Article 31 of the Euratom Treaty: Recommended radiological protection criteria for the clearance of buildings and building rubble from the dismantling of nuclear installations, Radiation protection 113 (2000).

[19] M.F. l'Annunziata, ed., Handbook of Radioactivity Analysis, Academic Press, 2012.

[20] A. Flammersfeld, Naturwissenschaften 33 (1946) 280; Z. Naturforsch. 2a (1947) 370.

[21] G.F. Knoll, Radiation Detection and Measurement, John Wiley & Sons, 2010.

[22] A. Kumar, A.J. Waker, An experimental study of the relative response of plastic scintillators to photons and beta particles, Radiat. Meas. 47 (2012) 930–935.

690 [23] Saint-Gobain Crystals, Premium Plastic Scintillators. Plastic Scintillators Data Sheet.
691 http://www.crystals.saint-gobain.com/.
692 [24] Z. Laili and al., “Genie TM 2000 Spectroscopy Software Operations,” *Canberra*, vol.
693 52, no. 1. pp. 1–361, 2016.
694 [25] LEA, Catalogue des sources ponctuelles et étendues,
695 http://www.lea-sources.com/fr/catalogue/sources-ponctuelles-eten.html.
696 [26] Pacific Northwest National Laboratory, Compendium of Material Composition Data
697 for Radiation Transport Modeling, Revision 1, 2011.
698 [27] Joint Evaluated Fission and Fusion 3.1.1 library, Java-based Nuclear Data Information
699 System (JANIS 4.0), Nuclear Energy Agency, 2013.
700 [28] J.A. Halbleib, R.P. Kensek, G.D. Valdez, S.M. Seltzer, M.J. Berger, ITS: The
701 Integrated Tiger Series Of Electron/Photon Transport Codes - Version 3.0, IEEE Trans. Nucl.
702 Sci. 39 (1992) 1025–1030.
703 [29] D.P. Gierga, K.J. Adams, Electron/Photon verification calculations using MCNP4B.
704 LA-13440 (1999).
705 [30] R. Jeraj, P.J. Keall, P.M. Ostwald, Comparisons between MCNP, EGS4 and
706 experiment for clinical electron beams, Phys. Med. Biol. 44 (1999) 705–717.
707 [31] D.R. Schaart, J.T.M. Jansen, J. Zoetelief, P.F.A. de Leege, A comparison of MCNP4C
708 electron transport with ITS 30 and experiment at incident energies between 100 keV and 20
709 MeV: Influence of voxel size, substeps and energy indexing algorithm, Phys. Med. Biol. 47
710 (2002) 1459–1484.
711 [32] T. O’Haver, Matlab peak fitting program,
712 https://terpconnect.umd.edu/~toh/spectrum/InteractivePeakFitter.htm
713 [33] Technical Committee ISO/TC 85, Nuclear energy. Subcommittee SC 2, Radiation
714 protection. Determination of the Characteristic Limits (decision Threshold, Detection Limit

715 and Limits of the Confidence Interval) for Measurements of Ionizing Radiation--fundamentals
716 and Application. ISO; 2010.
717 [34] SIBELCO, Properties of NE34 sand, https://www.couleur-
718 pigment.fr/WebRoot/ce_fr2/Shops/288750/5890/508B/11BF/4EAE/EB53/C0A8/1910/EF90/f
719 iche-technique-sable-de-quartz.pdf
720 [35] British Plastics Federeation, Polyethylene (Low Density) LDPE,
721 http://www.bpf.co.uk/Plastipedia/Polymers/LDPE.aspx
722 [36] British Plastics Federeation, Polyethylene (High Density) HDPE,
723 http://www.bpf.co.uk/Plastipedia/Polymers/HDPE.aspx

Figures

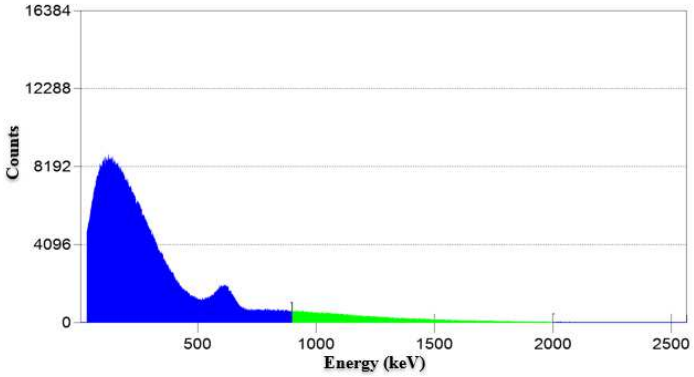

Fig. 1. Example of the energy spectrum of β– particles emitted by a ^{90}Sr and ^{137}Cs source after subtraction of the contribution from gamma photons.

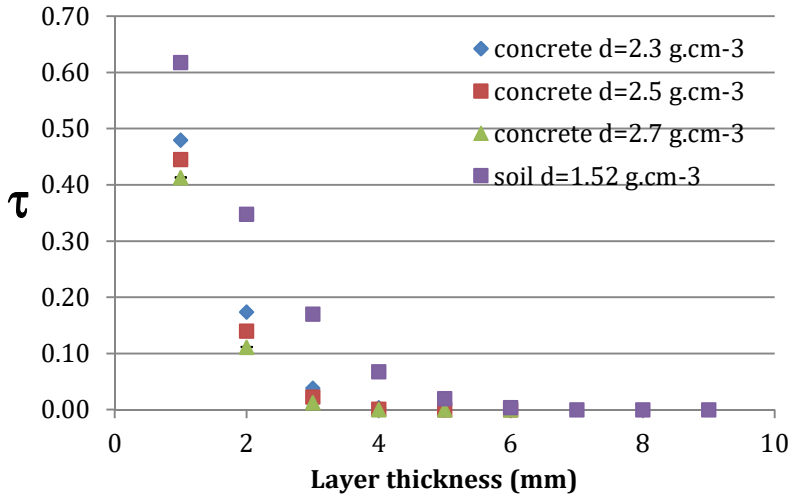

Fig. 2. Proportion τ of ^{90}Sr/^{90}Y electrons traveling through layers of concrete and soil with different densities as a function of the thickness of the layer.

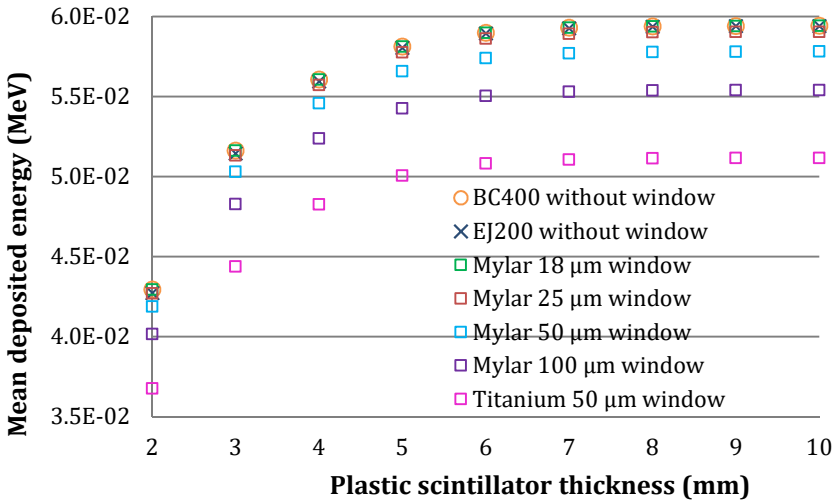

Fig. 3. Mean energy deposited by $^{90}Sr/^{90}Y$ electrons as a function of the thickness of the scintillator for two scintillating plastics, BC400 and EJ200 without window and when the EJ200 scintillator is covered by a layer of Mylar film (four different thicknesses) or a titanium sheet.

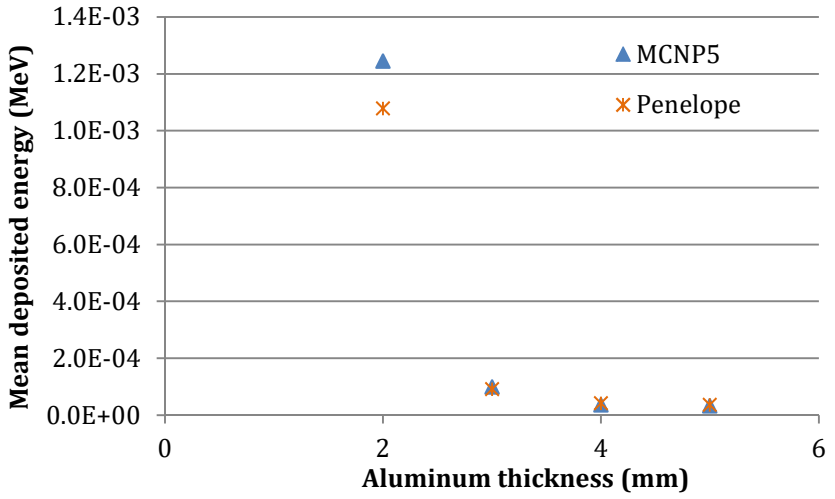

Fig. 4. Mean energy deposited by $^{90}Sr/^{90}Y$ electrons in the scintillator as a function of the thickness of the aluminum cover: comparison of the values obtained by MCNP5 and PENELOPE simulations.

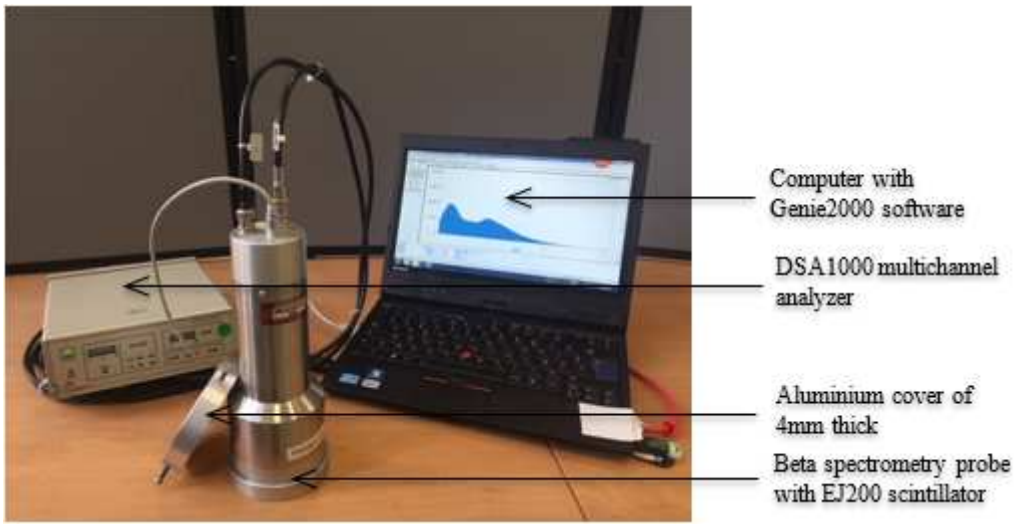

Fig. 5. Photographs of the device for beta spectrometry.

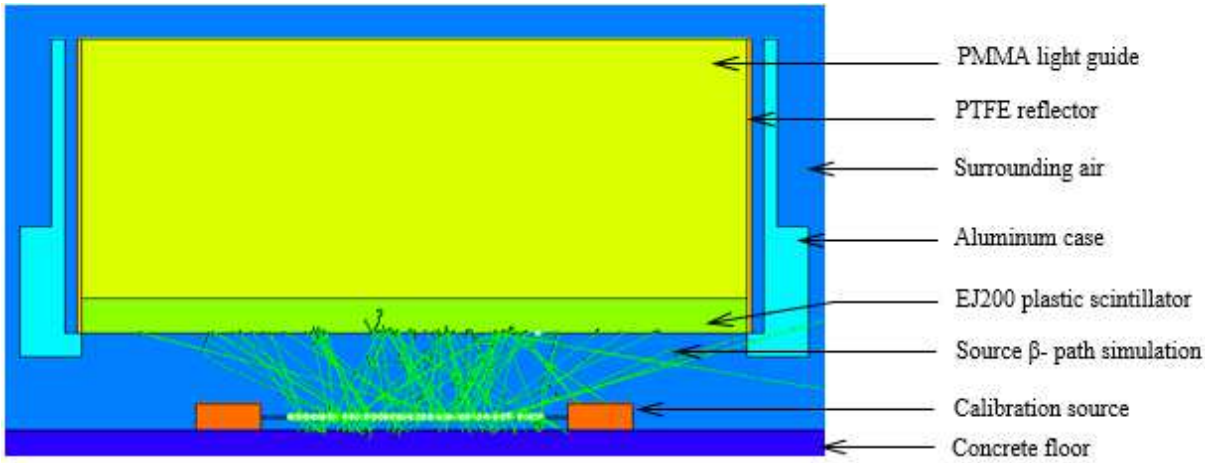

Fig. 6. Diagram of the setup and simulated electron paths in MCNP6 with a ^{137}Cs calibration source.

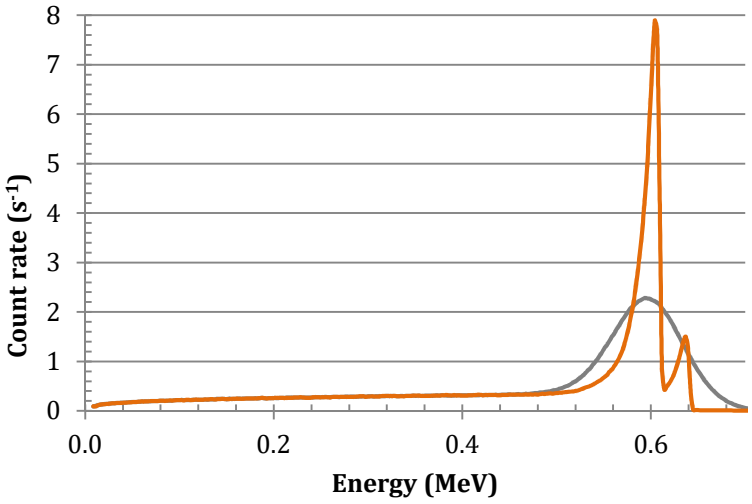

Fig. 7. Comparison of the simulated energy distributions in the scintillator arising from the internal conversion electrons emitted by ^{137}Cs at 624 and 656 keV accounting (grey line) or not (orange line) for the finite resolution of the detector.

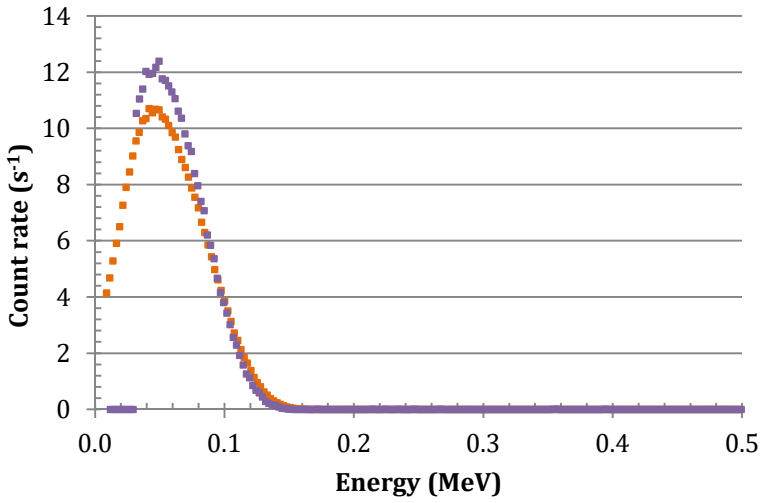

Fig. 8. Comparison of the simulated (in orange) and experimental (in purple) β– spectra of the ^{14}C calibration source. Electron transport was simulated using the integrated Tiger series (ITS) algorithm.

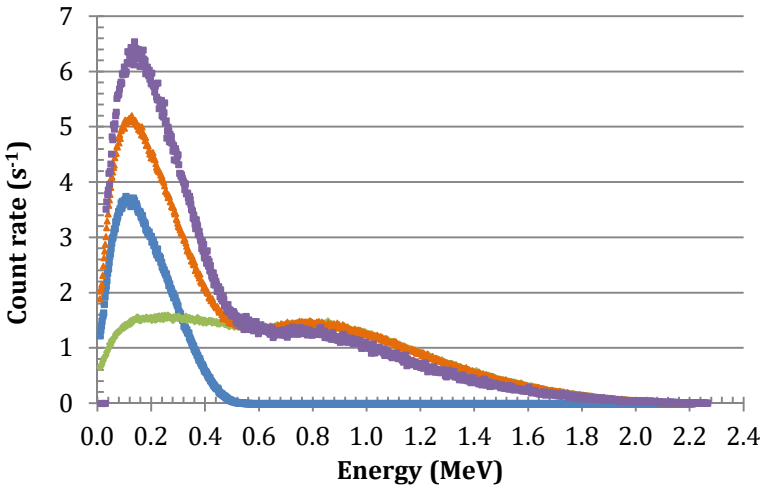

Fig. 9. Comparison of the simulated (in blue, the β- spectrum of ^{90}Sr, in green, the β- spectrum of ^{90}Y, in orange the total spectrum) and experimental (in purple) β– spectra of the ^{90}Sr/^{90}Y calibration source.

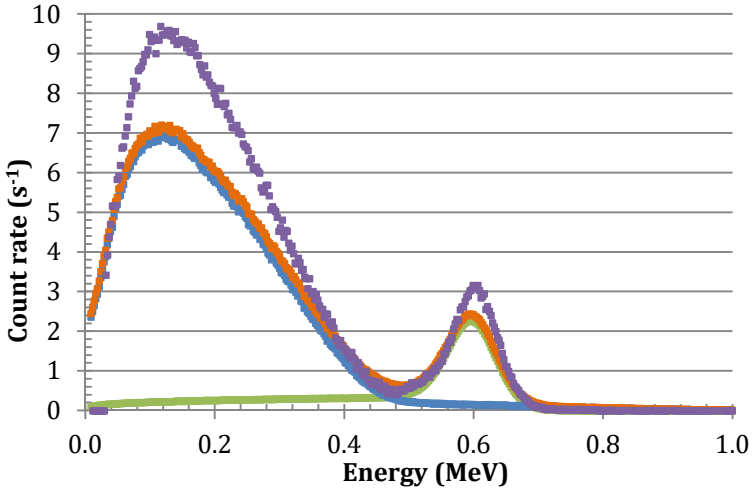

Fig. 10. Comparison of the simulated (in blue, the β- spectrum of ^{137}Cs, in green, the Internal Conversion spectrum, in orange the total spectrum) and experimental (in purple) β– spectra of the ^{137}Cs calibration source. IC, internal conversion.

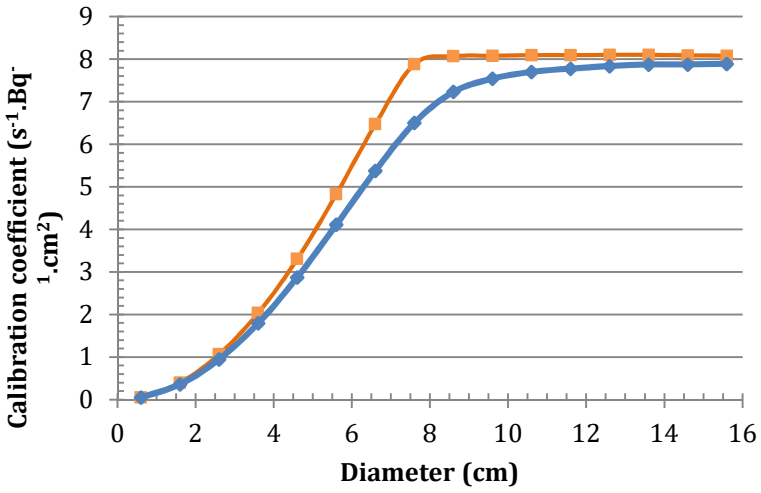

58

59 **Fig. 11.** Calibration coefficient in Eq. (2) for the energy interval 0.9–2.0 MeV as a function of
60 the diameter of a surface source of uniformly distributed activity in a concrete floor, with the
61 detector placed either in direct contact with the floor (orange line) or 4 mm above (blue line).

62

63

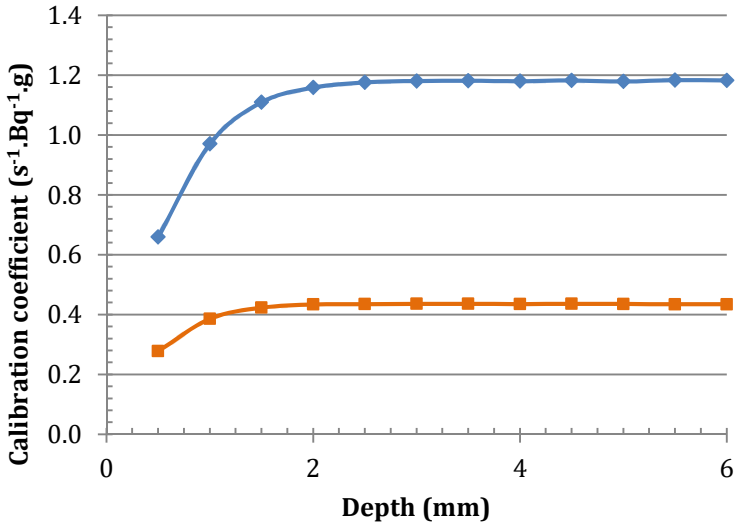

64

65 **Fig. 12.** Calibration coefficient in Eq. (2) for the two energy levels of interest (0.9–2.0 MeV
66 in blue, 1.2–2.0 MeV in orange) as a function of the depth of a uniformly distributed volume
67 source in concrete.

68

69

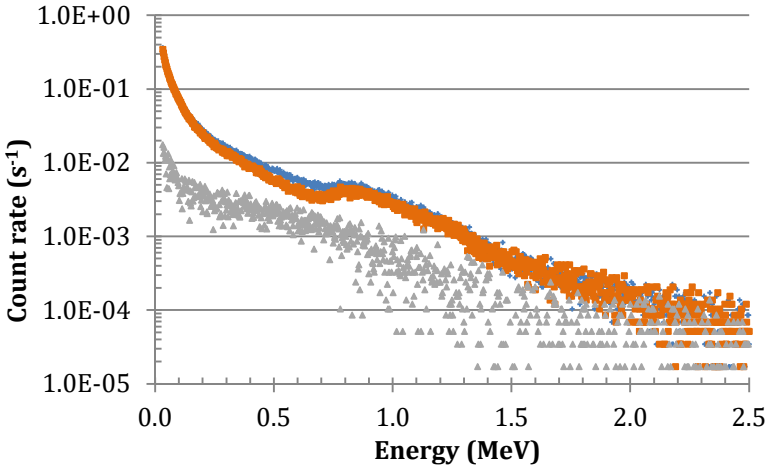

Fig. 13. Background spectra measured on non-contaminated concrete without the aluminum cover (in blue) and with (in orange), and the difference spectrum (in gray).

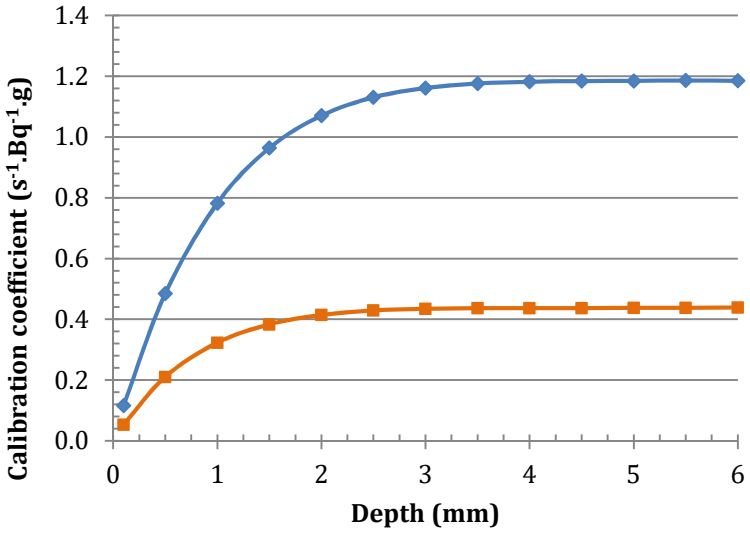

Fig. 14. Calibration coefficient in Eq. (2) for the two energy levels of interest (0.9–2.0 MeV in blue, 1.2–2.0 MeV in orange) as a function of the depth of a uniformly distributed volume source in Fontainebleau sand.

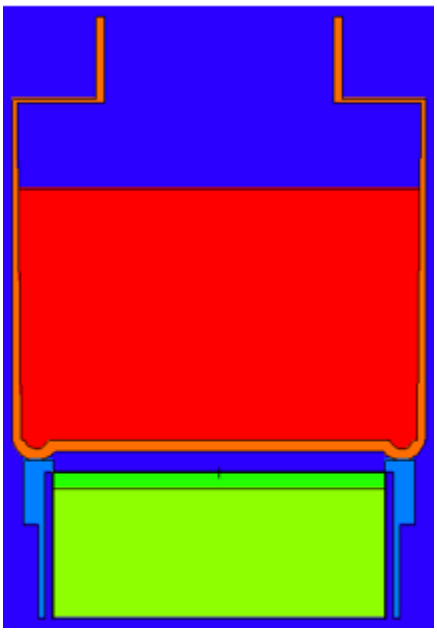

Fig. 15. Cross-section of the setup simulated in MCNP6 for measurements of ^{90}Sr activity in uniformly contaminated sand inside a standardized 500 cm^3 SG500 container.

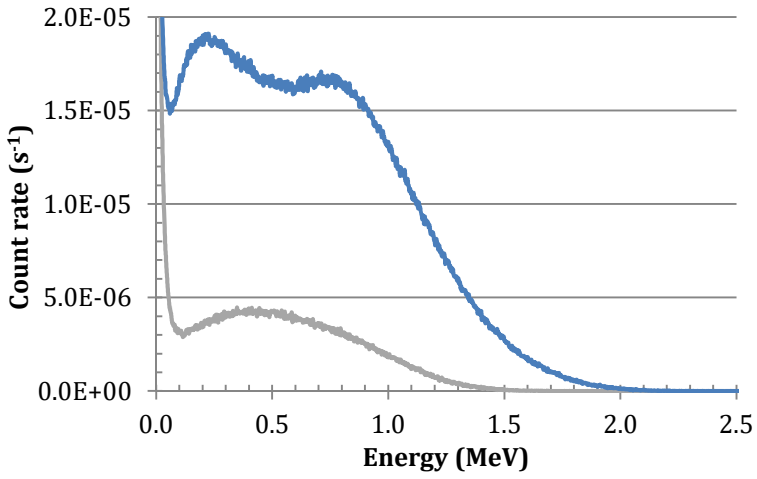

Fig. 16. Comparison of simulated ^{90}Sr/^{90}Y β– spectra of uniformly contaminated sand in a container with walls made of air (in blue) or polyethylene (in gray).

Fig. 17. Photographs of the beta spectrometer for measurements on sand samples in a standardized container (bottom left) and in direct contact with the sand (bottom right).

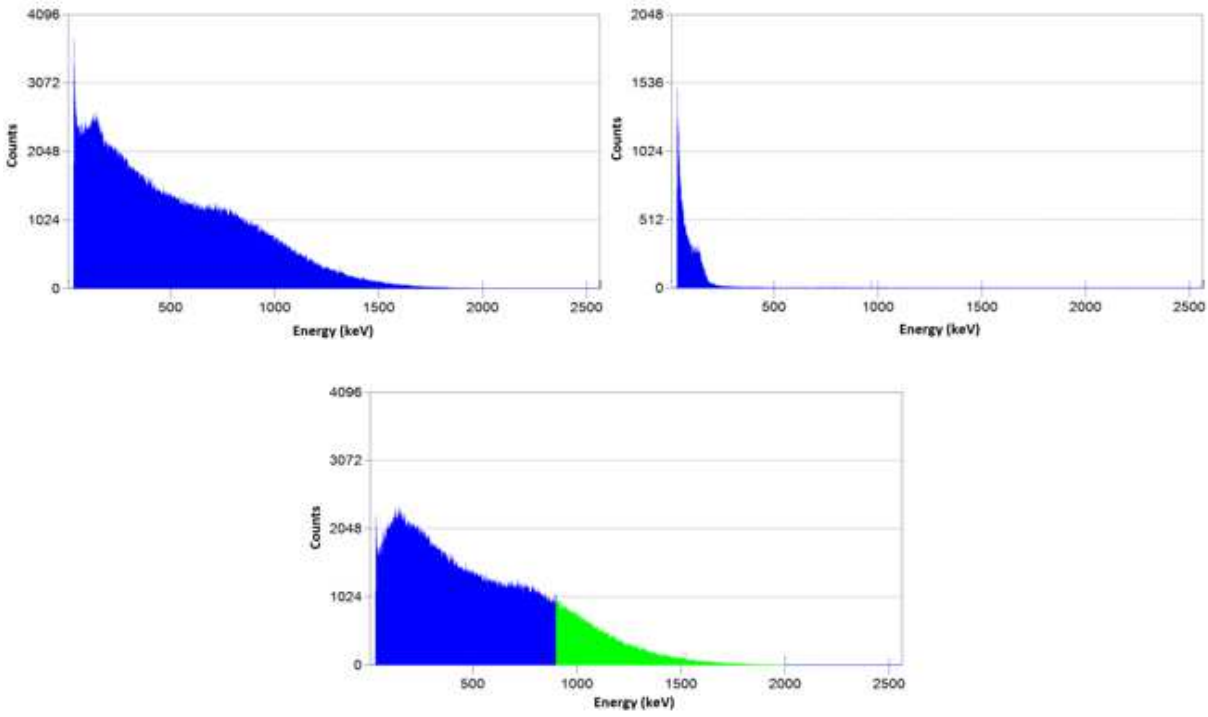

Fig. 18. Examples of the β spectra acquired in 10 min by the detector in direct contact with the sample 3 (Table 6): the main spectrum with beta and gamma components (upper left

panel), the auxiliary spectrum with only gamma component (upper right) and the final β spectrum (bottom panel) after subtraction of the latter from the former.

Tables

Table 1

Characteristics of the calibration sources used to validate the numerical model of the β spectrometer

Radionuclide	^{14}C	^{36}Cl	^{90}Sr	^{90}Y	^{204}Tl	^{137}Cs
Atomic number	6	17	38	39	81	55
Emission type	pure β–	pure β (98.1% β– & 1.9% β+ or EC)	pure β–	pure β–	pure β (97.08% β– & 2.92% β+)	β– & γ
Average energy (keV)	49.47	246.5	195.9	933	237.92	187.54
Maximum energy (keV)	156.47	709.3	546.2	2281.5	763.41	1175.1
Half life (years)	5.7×10^3	3.01×10^5	28.8	2.66 days	3.79	30.04
Activity	^{14}C	^{36}Cl	$^{90}Sr + ^{90}Y$		^{204}Tl	^{137}Cs
$A(t_0)$ (Bq)	1641	3269	3254		2839	3100
t_0	3 Mar 2015	1 Jul 2014	16 Jul 2014		4 Mar 2015	2 Mar 2015
$A(t1)$ (Bq)	1641	3269	3181		2685	3078
t_1	23 Jun 2015					

EC, electron capture.

Table 2

Comparison of the measured and simulated β spectra of the calibration sources

Radionuclide	Energy range (keV)	Average count rate (measured, {M})	Average count rate (simulated, {S})	Relative deviation ({S} – {M}) / {M}
^{14}C	31–156.5[a]	2.82×10^2	2.57×10^2	–9%
^{36}Cl	31–709.3[a]	1.39×10^3	1.09×10^3	–21%

^{204}Tl	31–763.4[a]	1.08×10^3	7.71×10^2	−29%
^{137}Cs	508–700[b]	1.17×10^2	1.02×10^2	−13%
^{90}Sr /^{90}Y	900–2000	2.03×10^2	2.55×10^2	+26%
^{90}Sr /^{90}Y	1200–2000	8.78×10^1	1.17×10^2	33%

[a]Total spectrum
[b]Internal conversion peak

Table 3

Calibration coefficient for different measurement setups determined by Monte Carlo simulations

Substrate[a]	Depth (mm)	Surface (cm^2)	Volume (cm^3)	Energy range (MeV)	C ($s^{-1}\cdot Bq^{-1}\cdot cm^2$)	C ($s^{-1}\cdot Bq^{-1}\cdot cm^3$)	C ($s^{-1}\cdot Bq^{-1}\cdot g$)
Concrete[a]	0	45.4	–	0.9–2.0	7.89	–	–
Concrete[a]	0	45.4	–	1.2–2.0	3.69	–	–
Sand[a]	0	45.4	–	0.9–2.0	7.95	–	–
Sand[a]	0	45.4	–	1.2–2.0	3.72	–	–
Concrete[a]	3	–	13.6	0.9–2.0	–	0.514	1.18
Concrete[a]	3	–	13.6	1.2–2.0	–	0.190	0.436
Sand[a]	4.5	–	20.4	0.9–2.0	–	0.790	1.19
Sand[a]	4.5	–	20.4	1.2–2.0	–	0.292	0.438
Sand[b]	58.3	–	388.16	0.9–2.0	–	–	1.177
Sand[b]	58.3	–	388.16	1.2–2.0	–	–	0.438
Sand[c]	58.3	–	388.16	0.9–2.0	–	–	0.143
Sand[c]	58.3	–	388.16	1.2–2.0	–	–	0.027
Sand[c]	58.3	–	388.16	0.3–2.0	–	–	0.661
Sand[d]	10	–	113.1	0.9–2.0	–	–	1.11 ± 60%

Sand[e]	58.3	–	388.16	0.3–2.0	–	–	0.61 ± 60%

[a]Placed in direct contact with the detector.
[b]Sand in 500cm^3 container with air walls
[c]Sand in 500cm^3 container with polyethylene walls
[d]Bare sand, detector covered by Parafilm M
[e]Sand in 500cm^3 container with polyethylene walls, detector covered by Parafilm M

Table 4

Detection limits calculated for different measurement times on non-contaminated cement

Energy range (MeV)	Count rate (s^{-1})	C ($s^{-1}\cdot Bq^{-1}\cdot g$)	DL, 2 × 10 min ($Bq\cdot g^{-1}$)	DL, 2 × 20 min ($Bq\cdot g^{-1}$)	DL, 2 × 30 min ($Bq\cdot g^{-1}$)	DL, 2 × 60 min ($Bq\cdot g^{-1}$)
0.9–2.0	7.13×10^{-2}	1.18	3.70×10^{-2}	2.60×10^{-2}	2.10×10^{-2}	1.50×10^{-2}
1.2–2.0	2.29×10^{-2}	0.436	5.60×10^{-2}	4.00×10^{-2}	3.30×10^{-2}	2.30×10^{-2}

C, calibration constant; DL, detection limit.

Table 5

Mass activities of samples of contaminated Fontainebleau sand as determined by radiochemical analysis

Sample	Year	$^{238}Pu+^{240}Pu$ ($Bq\cdot g^{-1}$)	^{238}Pu ($Bq\cdot g^{-1}$)	^{237}Np ($Bq\cdot g^{-1}$)	^{233}Pa ($Bq\cdot g^{-1}$)	^{137}Cs ($Bq\cdot g^{-1}$)	^{90}Sr ($Bq\cdot g^{-1}$)
1	2013	–	1.70 ± 0.73	2.00 ± 0.27	1.80 ± 0.21	–	27.0 ± 1.5
2	2013	–	21.0 ± 9.0	11.0 ± 0.9	11.00 ± 0.66	51.0 ± 3.0	190 ± 100
3	2015	–	4.5 ± 1.1	48.0 ± 5.0	43.0 ± 4.7	–	260 ± 140
4	2015	–	3.00 ± 0.75	67.0 ± 7.1	67.0 ± 7.7	–	560 ± 310
5	2013	–	32 ± 14	41.0 ± 4.4	43.0 ± 4.9	–	370 ± 200
6	2013	–	0.260 ± 0.024	0.099 ± 0.030	0.087 ± 0.015	–	76.0 ± 7.8
7	2013	$8.3 \pm 3.9 \times 10^3$	1.50 ± 0.15	5.5 ± 1.4	5.50 ± 0.35	–	210 ± 22
8	2013	$6.3 \pm 3.6 \times 10^3$	1.40 ± 0.12	5.1 ± 1.3	4.70 ± 0.30	170 ± 17	170.0 ± 8.6
9	2013	–	0.230 ± 0.023	0.90 ± 0.23	1.00 ± 0.07	–	9.40 ± 0.93
10	2013	–	0.036 ± 0.007	0.056 ± 0.018	0.071 ± 0.008	–	14.0 ± 0.14

The data are presented as A ± 2σ (activity ± twice the standard deviation).

29
30 **Table 6**

31 Comparison of the ^{90}Sr mass activity values obtained by radiochemical analysis and non-

32 destructive beta spectrometry for samples of contaminated Fontainebleau sand

Sample	Bare sand {A} ($Bq \cdot g^{-1}$)	Sand in SG500 {B} ($Bq \cdot g^{-1}$)	RA {C} ($Bq \cdot g^{-1}$)	({C}− {A}) / {C}	({C}− {B}) / {C}
1	25 ± 15	–	25 ± 14	0.4%	–
2	83 ± 50	–	180 ± 97	52.9%	–
3	16 ± 9.9	–	250 ± 140	35.0%	–
4	33 ± 20	70 ± 42	550 ± 300	39.5%	−28%
5	43 ± 26	–	340 ± 190	−23.9%	–
6	42 ± 25	11.0 ± 6.6	7.00 ± 0.73	40.5%	−57%
7	13.0 ± 7.6	–	200 ± 21	36.9%	–
8	9.5 ± 5.7	21 ± 13	160 ± 16	39.5%	−35%
9	6.2 ± 3.7	–	8.80 ± 0.86	29.0%	–
10	0.8 ± 0.5	1.9 ± 1.2	1.30 ± 0.13	37.4%	−51%

33 The data are presented as A ± 2σ (specific activity ± twice the standard deviation).
34 SG500, a standardized 500cm^3 polyethylene container; RA, radiochemical analysis.